Upconversion photoinduced electrochemiluminescence of luminol-H2O2 at Si/SiOx/Ni photoanodes

Yiran Zhao, Julie Descamps, Yoan Léger, Lionel Santinacci, Sandrine Zanna, Néso Sojic, Gabriel Loget

Upconversion Photoinduced Electrochemiluminescence of Luminol-H_2O_2 at Si/SiO_x/Ni Photoanodes

Yiran Zhao,[a] Julie Descamps,[b] Yoan Léger,[c] Lionel Santinacci,[d] Sandrine Zanna,[e] Neso Sojic,[b,*] Gabriel Loget[a,*]

a. Univ Rennes, CNRS, ISCR (Institut des Sciences Chimiques de Rennes)-UMR6226 - ScanMAT-UMS2001, F-35000 Rennes, France
*gabriel.loget@cnrs.fr

b. University of Bordeaux, Bordeaux INP, ISM, UMR CNRS 5255, 33607 Pessac, France
*sojic@u-bordeaux.fr

c. Univ Rennes, INSA Rennes, CNRS, Institut FOTON-UMR 6082, F-35000, Rennes, France.

d. CNRS, CINaM, Marseille, France

e. Chimie ParisTech – CNRS, PSL University, Institut de Recherche de Chimie Paris, Physical Chemistry of Surfaces Group, 11 rue Pierre et Marie Curie, 75005 Paris, France

Keywords

photoelectrochemistry, electrochemiluminescence, photoanodes, silicon, luminol

ABSTRACT

n-Si/SiO_x/Ni photoanodes are investigated for upconversion photoinduced electrochemiluminescence (PECL) employing the 3-aminophthalhydrazide (luminol)-hydrogen peroxide (H_2O_2) model electrochemiluminescent (ECL) system at pH 13. We show that IR excitation of the photoanode at 850 nm produces PECL emission at 440 nm resulting in an anti-Stokes shift of -410 nm at biases higher than 0 V vs Ag/AgCl. Due to the alkaline pH value of the electrolyte that prevents Ni dissolution, this upconverting system is active for a longer period (several hours) than the reported one for similar photoanodes operating at neutral pH. The PECL intensity can be controlled by the applied potential and the power density of the incident IR light. This new PECL system opens up promising perspectives for light-addressable electrodes, microscopy, and imaging.

1. Introduction

Electrochemiluminescence (ECL) is the generation of light in the vicinity of an electrode induced by an electrochemical reaction. This process involves a luminophore that is promoted to an excited state by an exergonic redox reaction, and which relaxes to the ground state by emitting a photon.[1,2] The ECL phenomenon is widely employed for medical diagnostics and clinical assays,[3–8] and research is currently progressing for microscopy[9–12] and imaging.[13–15] These applications rely mostly on the use of anodic luminophore-coreactant model systems such as tris(bipyridine)ruthenium(II) complex ($[Ru(bpy)_3]^{2+}$) with tripropylamine (TPA),[16] or 3-aminophthalhydrazide (luminol) with hydrogen peroxide (H_2O_2).[3]

Photoinduced ECL (PECL) is a category of ECL that is triggered at an illuminated semiconductor in depletion. In PECL, photons (λ_{em}) produced by the ECL reaction are

emitted under irradiation with an incident light (λ_{exc}).[17–19] In these conditions, photogenerated minority carriers (holes (h^+) in the case of an *n*-type semiconductor photoanode, or electrons (e^-) in the case of a *p*-type semiconductor photocathode)[20] drive the ECL reaction at an onset potential which is lower than that of a non-photoactive electrode[19,21,22] and the ECL can be localized on the electrode by focusing the incident light spot.[17,23,24] PECL can produce Stokes (with $\lambda_{em} > \lambda_{exc}$)[22,25] or anti-Stokes (i.e., upconversion type, with $\lambda_{em} < \lambda_{exc}$)[17,21,23,24] photon conversion depending on the experimental parameters, i.e., the semiconductor bandgap (E_g), the wavelength of the incident light (λ_{exc}), and the ECL system.[19] Such benefits make PECL a promising phenomenon for infrared (IR) imaging, bioanalysis, and for investigating photoelectrodes employed in solar energy conversion applications such as photoelectrochemical water splitting.[26–28]

Silicon (Si) is a particularly appropriate semiconductor for anti-Stokes PECL due to its abundance and its narrow bandgap (E_g = 1.1 eV, indicated as a dashed line in **Figure 1a**) allowing to use λ_{exc} up to the near IR. However, when employed in the oxidation regime with the aforementioned model aqueous ECL systems, Si photoanodes are subject to passivation.[29,30] Applying a protective coating onto Si is a strategy to solve this problem,[31,32] and several publications have reported outstanding properties of Si photoanodes stabilized with thin films based on Ni for the water oxidation reaction at high pH.[33–38] Inspired by this research, our group reported the anti-Stokes PECL in aqueous electrolyte using metal-insulator-semiconductor (MIS) photoanodes comprising a *n*-type Si (*n*-Si) absorber substrate, a SiO_x tunnel layer and a protective Ni thin film (the photoanode is denoted as *n*-Si/SiO_x/Ni) operated with the $[Ru(bpy)_3]^{2+}$-TPA model system.[21] A drawback of this system is that it requires the application of relatively high overpotentials > 0.5 V under IR illumination (all potentials in this article are referred *vs* Ag/AgCl).[21] Furthermore, to work efficiently, the $[Ru(bpy)_3]^{2+}$-TPA ECL system must be operated at physiological pH,

which favors the dissolution of the Ni thin film,[39] causing the photoanode degradation after a few tens of minutes.[21] The stability issue at neutral pH has been recently addressed by replacing the Ni coating with a noble metal such as Ir or Pt.[24] However, in addition to the high price of these materials, it still implies the use of relatively high (> 0.4 V) overpotentials. Another strategy to prevent Ni dissolution is to use an alkaline ECL system, for instance, luminol-H_2O_2, which is typically employed in 0.1 M KOH or NaOH solutions. At this pH, Ni is anodically stable and remains on the *n*-Si substrate.[39] Another benefit of this system is that it emits at a shorter wavelength (~440 nm) compared to $[Ru(bpy)_3]^{2+}$-TPA (~625 nm), allowing for larger anti-Stokes shifts, as shown in **Figure 1a**. Previous works related to the PECL of this system have been reported. First, the amplification of luminol ECL at glassy carbon electrodes illuminated above 500 nm has been observed by Cao *et al.*[40] Second, Vogel *et al.* have reported the PECL of luminol-H_2O_2 at *n*-Si photoanodes covalently modified with protecting 1,8-nonadiyne monolayers.[23] In this article, we study the PECL of luminol-H_2O_2 with *n*-Si/SiO_x/Ni photoanodes, we report that this system is suitable for converting light with an anti-Stokes shift of -410 nm (**Figure 1a**) at a low onset potential and that it retains its activity for hours.

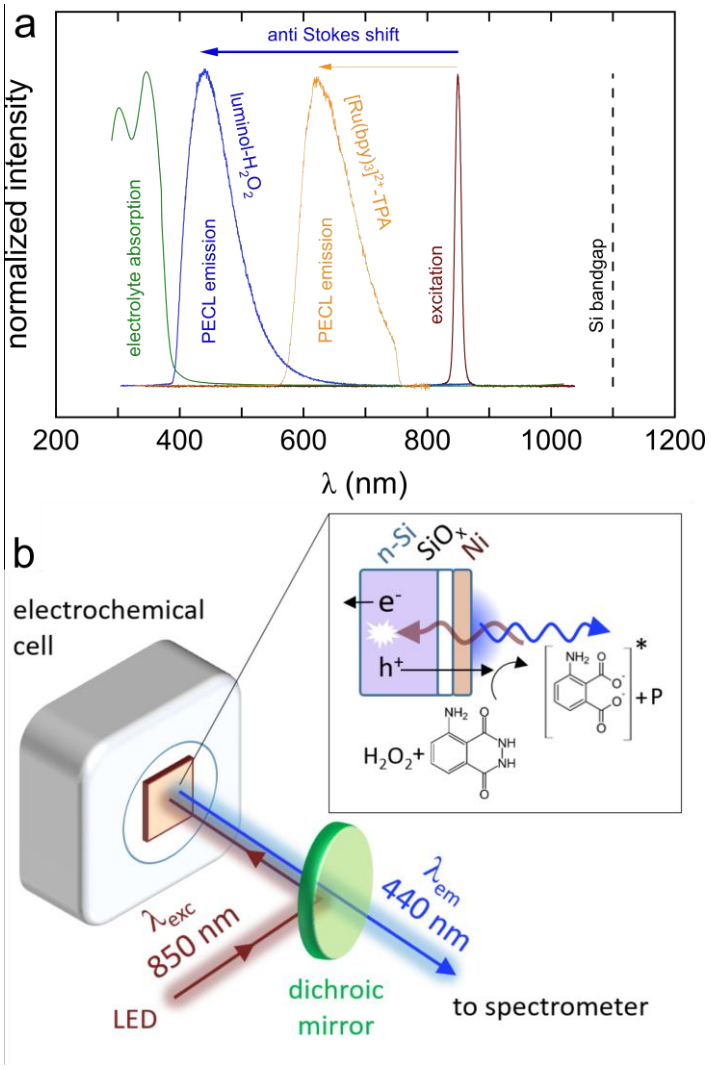

Figure 1. a) Normalized spectra: electrolyte absorption (10 mM luminol, 33 mM H_2O_2 (pH = 13)) (green curve), luminol PECL emission (blue curve), infrared excitation (brown curve), and Si bandgap position (black dashed curve). The normalized PECL emission spectra of the $[Ru(bpy)_3]^{2+}$-TPA system at similar photoanodes under 850 nm illumination is also shown (orange curve). Corresponding anti-Stokes shifts are shown by blue and orange arrows. b) Scheme showing the photoelectrochemical setup employed for the PECL study. Inset: charge transfer process at the electrode with the luminol-H_2O_2 ECL system.

2. Materials and methods

2.1. Materials and reagents

The *n*-type silicon wafers (1-10 Ω cm resistivity, phosphorus-doped, single side polished, 475-525 μm) (100) and the p^{++}-type silicon wafers (0.001-0.005 Ω cm resistivity, boron-doped, single side polished, 490-510 μm) (100) were purchased from University Wafers.

Acetone (MOS electronic grade, Erbatron from Carlo Erba) and anhydrous ethanol (RSE electronic grade, Erbatron from Carlo Erba) were used without further purification. The ultrapure water had a resistivity of 18.2 MΩ cm (Purelab Classic UV). Sulfuric acid (96%, VLSI grade Selectipur) and hydrogen peroxide (30%, VLSI, Sigma-Aldrich) were purchased from BASF and Sigma Aldrich, respectively. Luminol was purchased from Sigma-Aldrich.

2.2. Synthesis and characterization of the surfaces

The silicon wafers (p^{++}-type and *n*-type) were degreased by sonication in acetone, ethanol, and ultrapure water for 10 min respectively. The Si surfaces were then decontaminated and oxidized in piranha solution at 105 °C for 30 min to chemically form a ~1.5 nm-thick SiO_x layer, followed by rinsing with copious amounts of ultrapure water and dried under Ar flow. The Ni thin films were deposited on the cleaned *n*-Si/SiO_x surfaces by sputtering with a Leica EM ACE600 coating system (Ni target purity: 99.99%, Leica). The growth of the Ni film was controlled *in situ* using a quartz crystal microbalance, and the thickness (~2 nm) was measured *ex-situ* by atomic force microscopy (AFM). AFM pictures were acquired on an NT-MDT Ntegra microscope in semi-contact mode with FM tips (APPNANO, SPM Probe Model: FORTA-50, resonance frequency: 43-81 kHz). The images were treated and analyzed with the open-source Gwyddion software. Note that in the AFM picture shown in **Figure 2a**, to have a better view of most of the surface, the z-scale was restricted from 0 to 1.5 nm (the small white dots have a maximum height of ~5 nm). The chemical composition of the outermost surface was determined by X-ray photoelectron spectroscopy (XPS) using a VG ESCALAB 250 Xi spectrometer (ThermoFisher Scientific). Survey spectra were collected at a take-off angle of 90° and a pass energy of 100, using an Al Kα monochromated X-ray source.

2.3. Photoelectrochemical measurements

The uncoated and coated surfaces Si surfaces (1.3 x 1.3 cm²) were processed to fabricate the electrodes, first by making a backside Ohmic contact with InGa (99.99%, Alfa Aesar), Ag paste (Conductive Silver, Electron Microscopy Sciences), and Cu tape (Advanced Tapes AT526). Cyclic voltammetry, chronoamperometry (CA), chronopotentiometry (CP), and open circuit potential (OCP) measurements were performed with a Biologic SP-300 potentiostat connected to a 3-electrodes cell. The Si surface electrode was sealed with an O-ring on the backside of a homemade Teflon cell, which is also composed of a transparent glass window on the front side for transmitting light. In this cell, two holes are located on both sides, which are used for electrolyte renewal with a peristaltic pump (Grothen G728-1). The working electrode was the Si-based electrode with a fixed active area of 0.5 cm^2, the reference electrode was a 3 M NaCl Ag/AgCl electrode and the counter electrode was a carbon rod. The photoelectrochemical setup is schematized in **Figure 1b** and was previously described elsewhere.[24] The infrared light (a 850 nm light emitting diode (LED) (Thorlabs M850L3) cleaned by a 850 ±10 nm band-pass filter) was reflected onto the electrode surface by an 805 nm dichroic mirror (Thorlabs DMSP805R) and the PECL light was transmitted through the dichroic mirror, filtered by a 750 nm low-pass filter, to an optical fiber coupled with a spectrometer (Ocean Optics FLAME-T-VIS-NIR-ES or Princeton Instruments SpectraPro 2300i) for spectral acquisition. The aqueous electrolyte was composed of 10 mM luminol, 33 mM H_2O_2, and 0.1 M KOH or 0.1 M NaOH, in both cases the pH was ~13 (value measured for the ECL electrolyte = 12.85).

3. Results and discussion

3.1. Surface characterization

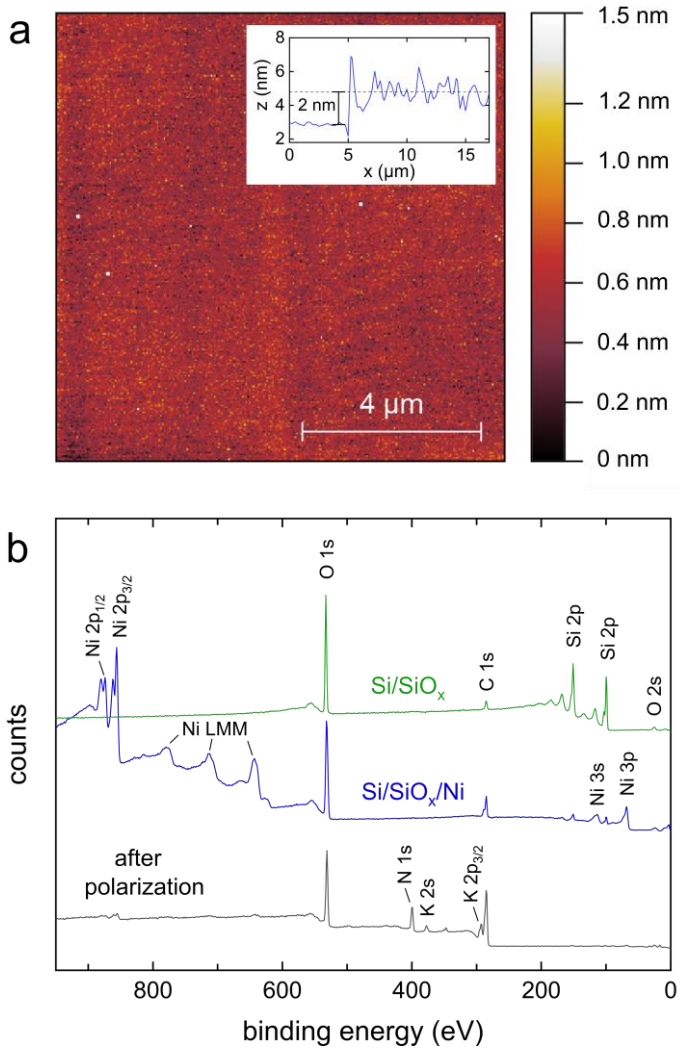

Figure 2. a) AFM picture of p^{++}-Si/SiO_x/Ni. Inset: AFM height profile of the Ni thin film onto p^{++}-Si/SiO_x after a lift-off process. b) XPS survey spectra of p^{++}-Si/SiO_x (green), p^{++}-Si/SiO_x/Ni (blue), and *n*-Si/SiO_x/Ni (black) after potentiostatic polarization at 0.2 V for 4.5 h under IR illumination in the ECL electrolyte.

The Si/SiO_x/Ni electrodes were prepared by chemical oxidation of a p^{++}-Si(100) or a *n*-Si(100) wafer followed by DC magnetron sputtering, as previously described.[21,24,36] After the sputtering of the ~2 nm-thick Ni film on p^{++}-Si/SiO_x, (Inset of **Figure 2a**) AFM was employed to assess the morphology of the deposited Ni coating. **Figure 2a** shows that the

film is mainly homogeneous with a root mean square roughness value of 134.3 pm, as determined from this AFM picture. The composition of the outermost surface was investigated by XPS before (**Figure 2b**, green spectrum) and after (**Figure 2b**, blue spectrum) deposition of the Ni thin film. The green spectrum shows that Si/SiO_x is only composed of Si and O atoms and has a low content of adventitious carbon. Previously published transmission electron microscopy cross-section analyses revealed that the so-prepared SiO_x layer has a thickness comprised between 1 and 2 nm.[36,41,42] The blue XPS spectrum, recorded after deposition of the Ni thin film, presents the characteristics of a dense and homogeneous Ni thin film onto the SiO_x layer. This is seen by the presence of the two intense Ni $2p_{3/2}$ and Ni $2p_{1/2}$ peaks at 855 and 873 eV (associated with their corresponding satellite peaks at 862 and 880 eV), the Auger Ni peaks between 620 and 800 eV, the Ni 3s peak at 113 eV, the Ni 3p peak at 68 eV,[43] and the vanishing of the Si 2p and 2s peaks at 99 and 150 eV. The presence of O 1s peak at 530 eV originates mainly from the native Ni oxide/hydroxide. The presence of this native layer is confirmed by the binding energy values of the Ni 3s, Ni $2p_{3/2,}$ and Ni $2p_{1/2}$ peaks.[43,44] The analysis of the XPS element fine spectra is described in detail in the supporting information. The analysis of the Ni 2p and the O 1s regions (**Figure S1a,b**) shows that the Ni film is mainly composed of NiO and $Ni(OH)_2$, produced by natural oxidation under the ambient condition of this ultrathin Ni thin film. For simplification, we nevertheless refer to these electrodes as *n*-Si/SiO_x/Ni. The black XPS spectrum was measured on a *n*-Si/SiO_x/Ni photoanode after a long-term polarization and will be discussed later.

3.2. Electrochemiluminescence (ECL)

First, electrochemistry was investigated in the dark on degenerate p^{++}-Si/SiO_x/Ni anodes to exclude photoinduced effects. p^{++}-Si, highly doped with boron atoms, was used as a substrate because it behaves as a conductor, and allows to perform electrochemical study without illumination. **Figure 3a** shows cyclic voltammograms (CVs) recorded at pH 13 for both ECL

reactants separately. The oxidation of luminol is shown by the red curve and the oxidation of H_2O_2 is shown by the purple curve. These CVs exhibit a large difference between the two oxidation onset potentials, H_2O_2 oxidation starts at -0.05 V and luminol oxidation at 0.2 V. In **Figure 3b**, the two ECL reactants (10 mM luminol + 33 mM H_2O_2) are studied together on a Ni-free p^{++}-Si/SiO_x anode (green curve) and a p^{++}-Si/SiO_x/Ni anode (blue curve), **Figure 3c** displays the corresponding ECL intensity. p^{++}-Si/SiO_x produces neither current nor ECL, suggesting that the charge transfer at the solid/liquid surface is inhibited by the insulating SiO_x layer. However, p^{++}-Si/SiO_x/Ni produces a large anodic current (j_{max} ~4 mA cm^{-2}) that starts at -0.06 V, coherent with the onset potential of H_2O_2 oxidation (**Figure 3a,** purple curve). On this electrode, ECL emission (**Figure 3c**, blue curve) starts only at a potential of 0.3 V, which is slightly more positive than the previously determined luminol oxidation onset potential (**Figure 3a**, red curve). It shows that ECL generation requires the oxidation of both H_2O_2 and luminol.

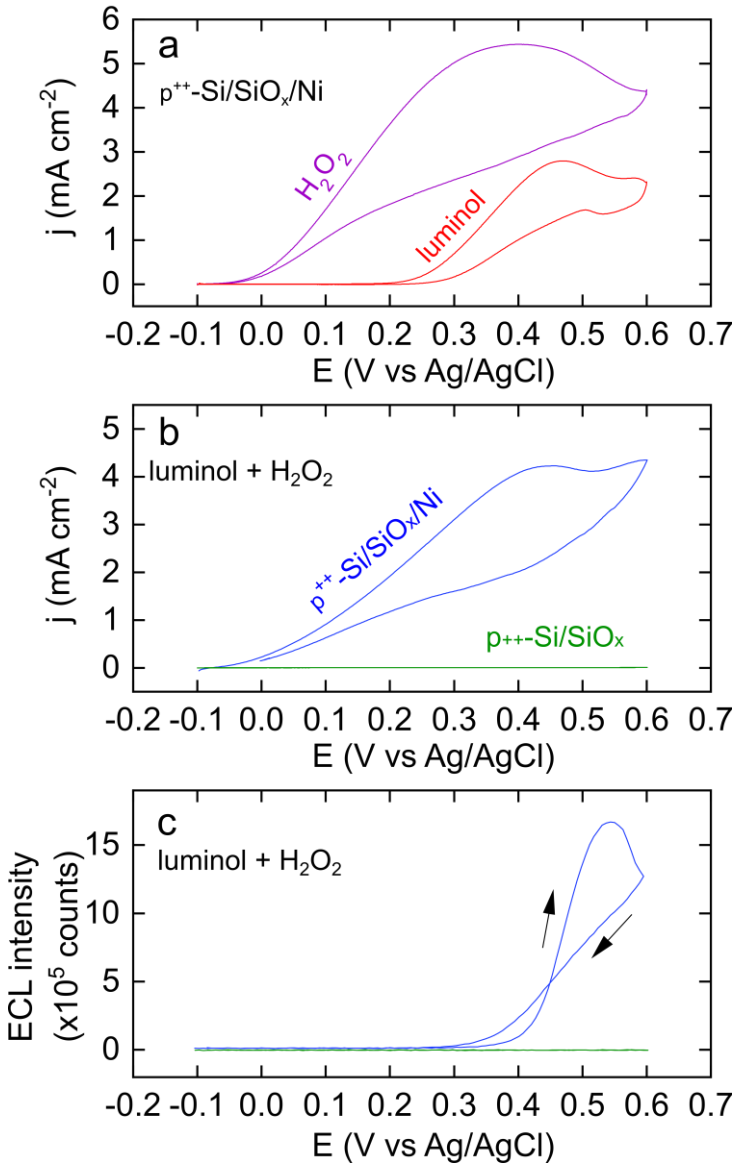

Figure 3. a) CVs recorded in the dark on p^{++}-Si/SiO_x/Ni in a pH 13 aqueous solution containing 33 mM H_2O_2 (purple curve) or 10 mM luminol (red curve). b) CVs recorded in the dark in both 33 mM H_2O_2 and 10 mM luminol (pH = 13) on p^{++}-Si/SiO_x/Ni (blue curve) and p^{++}-Si/SiO_x (green curve). c) Corresponding ECL intensity/potential profiles. Scan rate: 50 mV s^{-1}.

As schematized in the inset of **Figure 1b**, the ECL emission originates from the oxidation of H_2O_2 and luminol at the Ni surface, which induces a bond-breaking mechanism where the excited 3-aminophthalate* relaxes to the ground state by emitting a photon at 440 nm.

3.3. Photo-induced electrochemiluminescence (PECL)

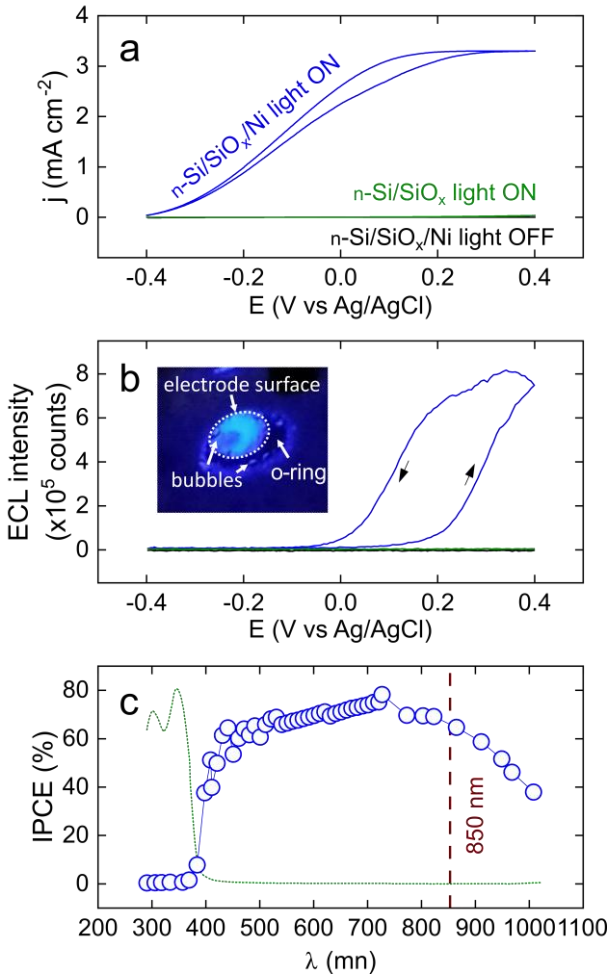

Figure 4. a) CVs recorded in the dark on *n*-Si/SiO_x/Ni (black) and under IR illumination on *n*-Si/SiO_x (green) and *n*-Si/SiO_x/Ni (blue). b) Corresponding ECL intensity-potential profiles. Scan rate: 50 mV s^{-1}, P_{LED}: 6.6 mW cm^{-2}. Inset: photograph of the surface during PECL emission. c) IPCE spectrum recorded on *n*-Si/SiO_x/Ni (blue) at 0.4 V, overlaid with the normalized electrolyte absorption (green dotted curve, data extracted from Figure 1a). The excitation wavelength is represented by a dashed brown line. Electrolyte composition: 10 mM luminol, 33 mM H_2O_2 (pH = 13).

Next, PECL was investigated in the same electrolyte (10 mM luminol and 33 mM H_2O_2 at pH 13) on *n*-Si/SiO_x/Ni surfaces prepared with a moderately doped and photoactive *n*-Si wafer. **Figure 4a** shows CVs recorded in the dark on *n*-Si/SiO_x/Ni (black curve) and under illumination at λ_{exc} = 850 nm with a power density (P_{LED}) of 6.6 mW cm^{-2} on *n*-Si/SiO_x (green

curve) and *n*-Si/SiO_x/Ni (blue curve). **Figure 4b** shows the corresponding ECL intensity profiles with the same color code. First, one can note that neither current nor ECL emission was recorded for *n*-Si/SiO_x under illumination, showing that hole transfer is not promoted to the electrolyte phase, which is consistent with the oxidation inhibition previously observed for p^{++}-Si/SiO_x (**Figure 3b,c** green curves). *n*-Si/SiO_x/Ni also fails in promoting charge transfer and, consequently, no ECL emission is detected in the dark (**Figure 4a,b** black curves). Conversely, under IR illumination, a photocurrent is generated, which starts at -0.4 V and reaches a plateau of ~3 mA cm^{-2} at 0.2 V. The maximum photocurrent density is lower than that recorded with p^{++}-Si/SiO_x/Ni electrode, suggesting that it is limited by the photon flux at high overpotential.[45] The simultaneously recorded PECL intensity starts around 0 V and increased considerably at ~0.2 V. With respect to the previous situation where ECL emission was triggered by oxidation of the reactants *via* the transfer of e^- from the liquid to the solid phase, in the present case PECL is generated *via* the interfacial transfer of photogenerated h^+, as shown in **Figure 1b**. It is interesting to note that the PECL curve displays a pronounced hysteresis, with the PECL emitted at the backward scan being more intense than that emitted at the forward scan. This may be partially attributed to the formation of a particularly active Ni oxide or hydroxide phase at the end of the forward scan as hysteresis was also observed for the ECL signal on p^{++}-Si/SiO_x/Ni, see **Figure 3c**. The fact that the PECL hysteresis is more pronounced than the ECL could be indicative of an adaptive-type junction having physical properties evolving during operation.[27,46] As was the case for ECL, the PECL emission can be easily seen with the naked eye, as shown in the digital photograph presented in the inset of **Figure 4b**. This image shows that bubbles, likely O_2 and N_2 (produced by H_2O_2 and luminol oxidation), evolved at the solid-liquid interface during PECL.

Photocurrent spectroscopy was also performed on *n*-Si/SiO_x/Ni. The blue curve of **Figure 4c** presents an incident photon-to-current conversion efficiency (IPCE) spectrum that was

recorded on *n*-Si/SiO_x/Ni at 0.4 V. This spectrum shows that the photoconversion efficiency is null in the near ultraviolet and starts to increase at λ_{exc} > 360 nm. The inactivity in the UV is caused by the electrolyte absorption, plotted as a green dotted curve in the same figure. The IPCE is higher than 40% in the visible range, reaches a maximum of ~75% at 725 nm, and varies from 69 to 38% from 800 to 1010 nm. The IPCE decrease is caused by the decrease of Si absorption coefficient at high wavelengths. At 850 nm (brown dashed line), which is the excitation wavelength employed in our PECL experiments, the IPCE is 65%, corresponding to a photocurrent density value of 3 mA cm^{-2} for an incident power of 6.6 mW cm^{-2},[47] in good agreement with the voltammetric measurements (**Figure 4a**, blue curve).

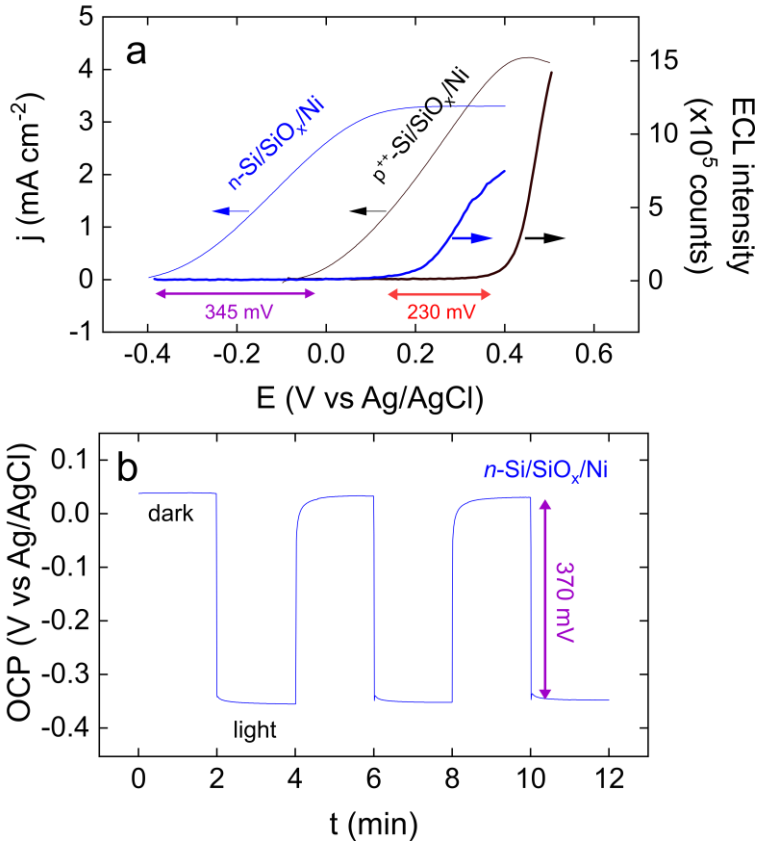

Figure 5. a) Voltammograms (thin curves) and corresponding ECL intensity/potential profiles (thick curves) recorded on p^{++}-Si/SiO_x/Ni in the dark (black curves) and *n*-Si/SiO_x/Ni under IR illumination (blue curves). Scan rate: 50 mV s^{-1}, P_{LED}: 6.6 mW cm^{-2}. b) OCP recorded as a function of time under intermittent IR illumination on *n*-Si/SiO_x/Ni. Electrolyte composition: 10 mM luminol, 33 mM H_2O_2 (pH 13).

Figure 5a overlays the voltammograms and the corresponding ECL intensity recorded during the forward scan at a p^{++}-Si/SiO_x/Ni anode (black curves) and a *n*-Si/SiO_x/Ni photoanode (blue curves). Due to the generation of a photovoltage, the current and the light emission at the *n*-Si/SiO_x/Ni photoanode starts at a lower onset potential than for the p^{++}-Si/SiO_x/Ni anode. **Figure 5b** presents the evolution of the open circuit potential (OCP) of a *n*-Si/SiO_x/Ni photoanode under intermittent IR illumination. On the first basis, the data presented in **Figure 5** allows performing three different estimations of the photovoltage (V_{oc}) value based on: *i*) the differences of onset potentials for current generation between p^{++}-Si/SiO_x/Ni and *n*-Si/SiO_x/Ni (**Figure 5a**, thin curves), *ii*) the difference of onset potential for ECL generation between p^{++}-Si/SiO_x/Ni and *n*-Si/SiO_x/Ni (**Figure 5a**, thick curves), and *iii*) the difference of dark and light OCP values at *n*-Si/SiO_x/Ni (**Figure 5b**). The difference in onset potentials for current generation and OCPs gave relatively similar V_{oc} values of 345 and 370 mV, respectively. However, the difference of onset potentials for ECL generation gave a much lower V_{oc} value of 230 mV, which may also be indicative of an adaptive behavior where chemical changes induced during the forward polarization affect the barrier height of the photovoltaic junction, affecting the effective photovoltage at high overpotentials.[27,46]

Then, the effect of the P_{LED} was investigated, as shown in **Figure 6a**. In this experiment, a constant potential of 0.4 V was applied to the *n*-Si/SiO_x/Ni photoanode in a flow cell (electrolyte flow = 1 mL s^{-1}). The IR illumination power density was varied from 0 to 5.2 mW cm^{-2} and the resulting current and PECL intensity were recorded. This figure shows that the photocurrent (black curve) and PECL intensity (colored disks) increase with P_{LED}. The colored disks of **Figure 6b** and the linear fit of this data (purple dashed curve) show that the PECL increase is relatively linear except for the lowest P_{LED} value (1 mW cm^{-2}).

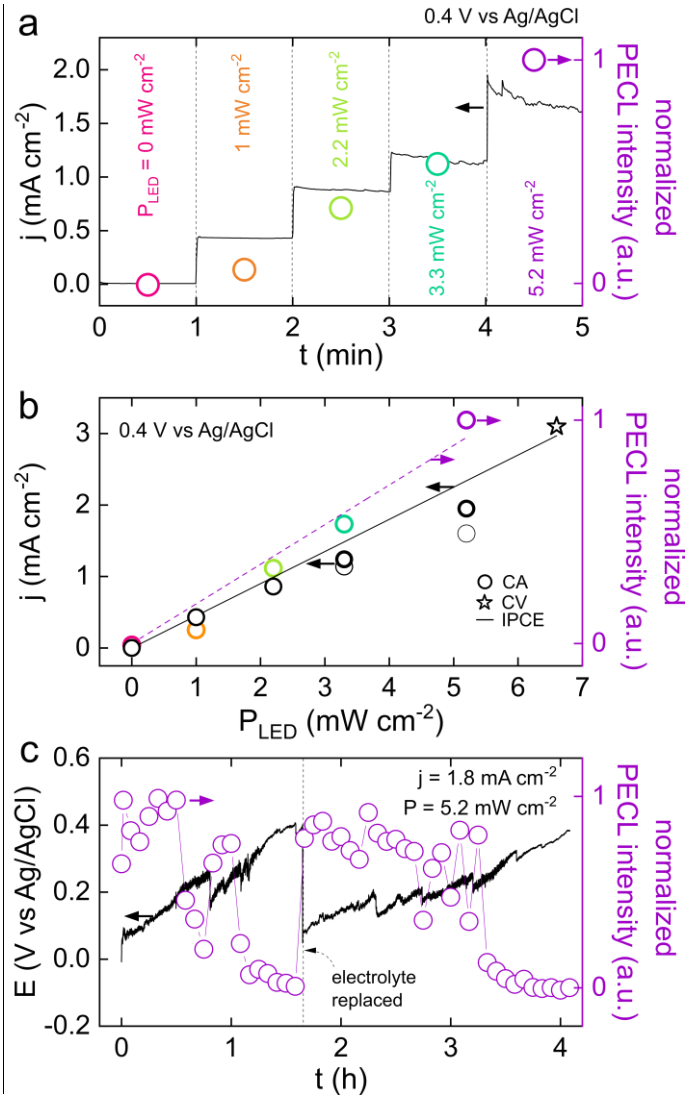

Figure 6. a) Chronoamperograms (black curve) and associated averaged PECL intensity (colored disks) recorded at 0.4 V on *n*-Si/SiO_x/Ni during the variation of P_{LED}. b) Plots of the photocurrent density (black data) and the PECL intensity (colored data) as a function of P_{LED}. Disks are experimental values extracted from panel a), thick black disks are *j* values recorded when P_{LED} has just been applied, the thin black disks are values recorded after 1 min of irradiation at P_{LED} = 3.3 and 5.2 mW cm^{-2}. The black star is the *j* value extracted from the CV of Figure 4a, the black curve represents the photocurrent variation expected from the experimentally determined IPCE, the dashed purple curve is a linear fit of the PECL data. c) Chronopotentiogram (black curve) and PECL intensity (purple disks) recorded on *n*-Si/SiO_x/Ni at *j* = 1.8 mA cm^{-2}, P_{LED}: 5.2 mW cm^{-2}, electrolyte flow rate: 1 mL s^{-1}. Electrolyte composition: 10 mM luminol, 33 mM H_2O_2 (pH 13).

It is also interesting to observe how P_{LED} affects the photocurrent density (**Figure 6b**, black data). Again, it seems that there is a quasi-linear relationship between these two parameters, which is well in line with a light-limited photocurrent density at this potential. Accordingly,

the *j* values extracted from the chronoamperograms of **Figure 6a** (**Figure 6b**, black disks), and the CVs of **Figure 4a** (**Figure 6b**, black star) are relatively close to that expected from the determined IPCE value of 65%, plotted in **Figure 6b** as a dotted black line. For the highest P_{LED} values, *j* decreased after 1 min of polarization (**Figure 6b**, thick and thin black disks for P_{LED} = 3.3 and 5.2 mW cm^{-2}), deviating from the value expected from IPCE. We attribute this decrease to the formation of bubbles at the electrode surface that reduces the active surface of the photoanode.

Finally, the PECL stability of this system was tested by applying a constant photocurrent of 1.8 mA cm^{-2} to the *n*-Si/SiO_x/Ni photoanode under IR illumination (P_{LED} = 5.2 mW cm^{-2}) while the potential and PECL intensity were recorded, as presented in **Figure 6c**. The black curve shows that the potential of the photoanode varied from 50 to 400 mV over the first 1.6 h. Although its intensity varied considerably, PECL was emitted during the first hour of the experiment. After ~1 h, PECL faded and vanished. To assess if the PECL decay was caused by the degradation of the *n*-Si/SiO_x/Ni photoanode or the electrolyte, the electrolyte was replaced at 1.6 h by a freshly prepared one, which immediately restored the initial potential value as well as the PECL intensity. After the electrolyte change, the electrode emitted PECL for ~1.5 h and a similar decay occurred, showing that PECL loss was caused by the consumption of the ECL reactants in the electrolyte. Strong variation in PECL intensity can be observed. For instance, at 0.5 h, the intensity decreases, and, at 0.8 h, increases suddenly. Shorter but similar profiles can be observed in the second part of the experiments (e.g., at 2.3 h). The fact that the PECL increases when the potential abruptly decreases suggests that such variations are caused by the release of O_2 and N_2 bubbles (as discussed previously), which alter the emission signal intensity. To get more insights into the evolution of the photoanode surface, *n*-Si/SiO_x/Ni was analyzed by XPS after a long polarization (4.5 h at 0.2 V). As

presented in **Figure 2b**, the 2p and 2s Si peaks were no longer observable and the intensity of the Ni 2p peaks considerably decreased. Interestingly, the intensity of the C 1s peak increased and new peaks attributed to N 1s (399 eV), K 2s at (378 eV) and K $2p_{3/2}$ (293 eV) appeared. The analysis of the XPS fine element Ni 2p, O 1s, N 1s, and C 1s spectra of the electrode after polarization is described in detail in the supporting information (**Figure S1a-d**). This suggests that prolonged polarization in this medium induces the precipitation of an insoluble coating composed of K^+ (initially present in the supporting electrolyte) and organics resulting from luminol degradation products. We expect that the formation of this layer will impede photoanode activity during longer experiments.

4. Conclusion

In this article, we have reported the anti-Stokes PECL of the luminol-H_2O_2 model ECL system operated in an alkaline electrolyte on *n*-Si/SiO_x/Ni photoanodes. Here, IR excitation of the photoanode at λ_{em} = 850 nm produces PECL emission at λ_{em} = 440 nm resulting in an anti-Stokes shift of -410 nm, which is the largest reported so far.[19,48] Due to the appropriate electrolyte pH, the system can be used for a longer time than that reported for similar photoanodes at neutral pH[21], as further confirmed experimentally (**Figure S2**), and exhibits a high IPCE. The PECL intensity can be controlled by simple physical parameters such as the applied potential and the power density of the incident IR light. According to voltammograms and OCP measurements, the photovoltage of *n*-Si/SiO_x/Ni in this medium is ~360 mV, which is close to the 410 mV of our previous report.[21] However, the emission onset is only shifted by 230 mV when comparing the photoanode with a similar but non-photoactive anode. The electrode can be used for hours and PECL decay can be conveniently restored by replacing the electrolyte. Prolonged electrolysis showed that bubble evolution caused by the degradation of the ECL reactants produces variation in the PECL intensity. Due to the high

pH of the luminol-H_2O_2 ECL electrolyte, and the fact that the photoanode system is based on Si, we think that this report is promising for future fundamental research applied to solar energy conversion.[26,27,33–38]

Acknowledgments

This work is funded by ANR (LiCORN - ANR-20-CE29-0006). Sandrine Zanna (Chimie ParisTech, Paris) and Lionel Santinacci (CNRS, CINaM, Marseille) are warmly acknowledged for their help with XPS measurements and discussions.

REFERENCES

[1] N. Sojic, Analytical electrogenerated chemiluminescence: from fundamentals to bioassays, The Royal Society of Chemistry, 2020.

[2] Z. Liu, W. Qi, G. Xu, Recent advances in electrochemiluminescence, Chem. Soc. Rev. 44 (2015) 3117–3142.

[3] E. Sobhanie, F. Salehnia, G. Xu, Y. Hamidipanah, S. Arshian, A. Firoozbakhtian, M. Hosseini, M.R. Ganjali, S. Hanif, Recent trends and advancements in electrochemiluminescence biosensors for human virus detection, Trends Anal. Chem. 157 (2022) 116727.

[4] F. Du, Z. Dong, Y. Guan, A.M. Zeid, D. Ma, J. Feng, D. Yang, G. Xu, Single-electrode electrochemical system for the visual and high-throughput electrochemiluminescence immunoassay, Anal. Chem. 94 (2022) 2189–2194.

[5] K. Sakanoue, A. Fiorani, C.I. Santo, Irkham, G. Valenti, F. Paolucci, Y. Einaga, Boron-doped diamond electrode outperforms the state-of-the-art electrochemiluminescence from microbeads immunoassay, ACS Sensors. 7 (2022) 1145–1155.

[6] X. Ma, W. Gao, F. Du, F. Yuan, J. Yu, Y. Guan, N. Sojic, G. Xu, Rational design of electrochemiluminescent devices, Acc. Chem. Res. 54 (2021) 2936–2945.

[7] M. Bhaiyya, P.K. Pattnaik, S. Goel, A brief review on miniaturized electrochemiluminescence devices: From fabrication to applications, Curr. Opin. Electrochem. 30 (2021) 100800.

[8] Q. Kang, Y. Huang, X. Ma, M. Li, C. Ma, D. Shen, A simple and sensitive electrochemiluminescence spectrum measurement platform and spectrum-resolved ratiometric sensor for miroRNA-141 determination, Electrochim. Acta. 422 (2022) 140544.

[9] S. Voci, B. Goudeau, G. Valenti, A. Lesch, M. Jović, S. Rapino, F. Paolucci, S. Arbault, N. Sojic, Surface-confined electrochemiluminescence microscopy of cell membranes, J. Am. Chem. Soc. 140 (2018) 14753–14760.

[10] H. Ding, W. Guo, B. Su, Electrochemiluminescence single-cell analysis: intensity- and imaging-based methods, ChemPlusChem. 85 (2020) 725–733.

[11] S. Rebeccani, A. Zanut, C.I. Santo, G. Valenti, F. Paolucci, A guide inside electrochemiluminescent microscopy mechanisms for analytical performance improvement, Anal. Chem. 94 (2022) 336–348.

[12] M.-M. Chen, C.-H. Xu, W. Zhao, H.-Y. Chen, J.-J. Xu, Super-resolution electrogenerated chemiluminescence microscopy for single-nanocatalyst imaging, J. Am. Chem. Soc. 143 (2021) 18511–18518.

[13] C. Meng, S. Knežević, F. Du, Y. Guan, F. Kanoufi, N. Sojic, G. Xu, Recent advances in electrochemiluminescence imaging analysis, eScience. (2022).

[14] L. Xu, Y. Li, S. Wu, X. Liu, B. Su, Imaging latent fingerprints by electrochemiluminescence, Angew. Chem. Int. Ed. 51 (2012) 8068–8072.

[15] J. Dong, Y. Lu, Y. Xu, F. Chen, J. Yang, Y. Chen, J. Feng, Direct imaging of single-molecule electrochemical reactions in solution, Nature. 596 (2021) 244–249.

[16] N.E. Tokel-Takvoryan, R.E. Hemingway, A.J. Bard, Electrogenerated chemiluminescence. XIII. Electrochemical and electrogenerated chemiluminescence studies of ruthenium chelates, J. Am. Chem. Soc. 95 (1973) 6582–6589.

[17] D. Laser, A.J. Bard, Semiconductor electrodes. Photo-induced electrogenerated chemiluminescence and up-conversion at semiconductor electrodes, Chem. Phys. Lett. 34 (1975) 605–610.

[18] J.D. Luttmer, A.J. Bard, Electrogenerated Chemiluminescence: 34. Photo- Induced electrogenerated chemiluminescence and up- conversion at semiconductor electrodes, J. Electrochem. Soc. 126 (1979) 414–419.

[19] Y. Zhao, L. Bouffier, G. Xu, G. Loget, N. Sojic, Electrochemiluminescence with semiconductor (nano)materials, Chem. Sci. 13 (2022) 2528–2550.

[20] J. Descamps, Y. Zhao, J. Yu, G. Xu, Y. Léger, G. Loget, N. Sojic, Anti-Stokes photoinduced electrochemiluminescence at a photocathode, Chem. Commun. 58 (2022) 6686–6688.

[21] Y. Zhao, J. Yu, G. Xu, N. Sojic, G. Loget, Photoinduced electrochemiluminescence at silicon electrodes in water, J. Am. Chem. Soc. 141 (2019) 13013–13016.

[22] J. Yu, H. Saada, R. Abdallah, G. Loget, N. Sojic, Luminescence amplification at $BiVO_4$ photoanodes by photoinduced electrochemiluminescence, Angew. Chem. Int. Ed. 59 (2020) 15157–15160.

[23] Y.B. Vogel, N. Darwish, S. Ciampi, Spatiotemporal control of electrochemiluminescence guided by a visible light stimulus, Cell Rep. Phys. Sci. 1 (2020) 100107.

[24] Y. Zhao, J. Descamps, S. Ababou-Girard, J.-F. Bergamin, L. Santinacci, Y. Léger, N. Sojic, G. Loget, Metal-insulator-semiconductor anodes for ultrastable and site-selective upconversion photoinduced electrochemiluminescence, Angew. Chem. Int. Ed. (2022) e2022018.

[25] J. Yu, H. Saada, N. Sojic, G. Loget, Photoinduced electrochemiluminescence at nanostructured hematite electrodes, Electrochim. Acta. 381 (2021) 138238.

[26] G. Loget, B. Fabre, S. Fryars, C. Mériadec, S. Ababou-Girard, Dispersed Ni nanoparticles stabilize silicon photoanodes for efficient and inexpensive sunlight-assisted water oxidation, ACS Energy Lett. 2 (2017) 569–573.

[27] F.A.L. Laskowski, S.Z. Oener, M.R. Nellist, A.M. Gordon, D.C. Bain, J.L. Fehrs, S.W. Boettcher, Nanoscale semiconductor/catalyst interfaces in photoelectrochemistry, Nat. Mater. 19 (2020) 69–76.

[28] P. Nunez, M. Cabán-Acevedo, W. Yu, M.H. Richter, K. Kennedy, A.M. Villarino, B.S. Brunschwig, N.S. Lewis, Origin of the electrical barrier in electrolessly deposited platinum nanoparticles on p-si surfaces, J. Phys. Chem. C. 125 (2021) 17660–17670.

[29] H. Gerischer, Photodecomposition of semiconductors thermodynamics, kinetics and application to solar cells, Farad. Disc. Chem. Soc. 70 (1980) 137–151.

[30] K. Sun, S. Shen, Y. Liang, P.E. Burrows, S.S. Mao, D. Wang, Enabling silicon for solar-fuel production, Chem. Rev. 114 (2014) 8662–8719.

[31] A.G. Scheuermann, J.P. Lawrence, K.W. Kemp, T. Ito, A. Walsh, C.E.D. Chidsey,

P.K. Hurley, P.C. McIntyre, Design principles for maximizing photovoltage in metal-oxide-protected water-splitting photoanodes, Nat. Mater. 15 (2016) 99–105.

[32] S. Hu, M.R. Shaner, J.A. Beardslee, M. Lichterman, B.S. Brunschwig, N.S. Lewis, Amorphous TiO_2 coatings stabilize Si, GaAs, and GaP photoanodes for efficient water oxidation, Science. 344 (2014) 1005–1009.

[33] M.J. Kenney, M. Gong, Y. Li, J.Z. Wu, J. Feng, M. Lanza, H. Dai, High-performance silicon photoanodes passivated with ultrathin nickel films for water oxidation, Science. 342 (2013) 836–840.

[34] K. Sun, M.T. McDowell, A.C. Nielander, S. Hu, M.R. Shaner, F. Yang, B.S. Brunschwig, N.S. Lewis, Stable solar-driven water oxidation to O_2(g) by Ni-oxide-coated silicon photoanodes, J. Phys. Chem. Lett. 6 (2015) 592–598.

[35] F.A.L. Laskowski, M.R. Nellist, R. Venkatkarthick, S.W. Boettcher, Junction behavior of n-Si photoanodes protected by thin Ni elucidated from dual working electrode photoelectrochemistry, Energy Environ. Sci. 10 (2017) 570–579.

[36] G. Loget, C. Mériadec, V. Dorcet, B. Fabre, A. Vacher, S. Fryars, S. Ababou-Girard, Tailoring the photoelectrochemistry of catalytic metal-insulator-semiconductor (MIS) photoanodes by a dissolution method, Nat. Commun. 10 (2019) 3522.

[37] S. Lee, L. Ji, A.C. De Palma, E.T. Yu, Scalable, highly stable Si-based metal-insulator-semiconductor photoanodes for water oxidation fabricated using thin-film reactions and electrodeposition, Nat. Commun. 12 (2021) 3982.

[38] J. Ma, H. Chi, A. Wang, P. Wang, H. Jing, T. Yao, C. Li, Identifying and removing the interfacial states in metal-oxide–semiconductor schottky si photoanodes for the highest fill factor, J. Am. Chem. Soc. 144 (2022) 17540–17548.

[39] M. Pourbaix, Atlas of electrochemical equilibria in aqueous solutions, National Association of Corrosion Engineers, Houston, Tex., 1974.

[40] Z. Cao, B. Su, Light enhanced electrochemistry and electrochemiluminescence of luminol at glassy carbon electrodes, Electrochem. Commun. 98 (2019) 47–52.

[41] P. Aroonratsameruang, P. Pattanasattayavong, V. Dorcet, C. Mériadec, S. Ababou-Girard, S. Fryars, G. Loget, Structure–property relationships in redox-derivatized metal–insulator–semiconductor (MIS) photoanodes, J. Phys. Chem. C. 124 (2020) 25907–25916.

[42] J. Dabboussi, R. Abdallah, L. Santinacci, S. Zanna, A. Vacher, V. Dorcet, S. Fryars, D. Floner, G. Loget, Solar-assisted urea oxidation at silicon photoanodes promoted by an amorphous and optically adaptive Ni-Mo-O catalytic layer, J. Mater. Chem. A. 10 (2022) 19769–19776.

[43] C. D. Wagner, J. F. Moulder, L. E. R. Davis, W. M. Riggs, Handbook of X-ray photoelectron spectroscopy, 2008.

[44] N.S. McIntyre, M.G. Cook, X-ray photoelectron studies on some oxides and hydroxides of cobalt, nickel, and copper, Anal. Chem. 47 (1975) 2208–2213.

[45] W.W. Gärtner, Depletion-layer photoeffects in semiconductors, Phys. Rev. 116 (1959) 84–87.

[46] F. Lin, S.W. Boettcher, Adaptive semiconductor/electrocatalyst junctions in water-

splitting photoanodes, Nat. Mater. 13 (2014) 81–86.

[47] Z. Chen, T.G. Deutsch, H.N. Dinh, K. Domen, K. Emery, A.J. Forman, N. Gaillard, R. Garland, C. Heske, T.F. Jaramillo, A. Kleiman-Shwarsctein, E. Miller, K. Takanabe, J. Turner, Efficiency definitions in the field of PEC, in: Z. Chen, H.N. Dinh, E. Miller (Eds.), Photoelectrochemical water splitting: standards, experimental methods, and protocols, Ch. 2, Springer New York, New York, NY, 2013, p. 7–16.

[48] Y. Zhao, J. Descamps, B. Le Corre, Y. Léger, A. Kuhn, N. Sojic, G. Loget, Wireless anti-stokes photoinduced electrochemiluminescence at closed semiconducting bipolar electrodes, J. Phys. Chem. Lett. 13 (2022) 5538–5544.